Continuum to rarefied diffusive tortuosity factors in porous media from X-ray microtomography

Joseph C. Ferguson^a, Arnaud Borner^b, Francesco Panerai^{c,d}, Sigrid Close^e,
Nagi N. Mansour^{b,d}

a Dept. of Mechanical Engineering, Stanford University, Stanford, CA 94305
 b AMA Inc. NASA Ames Research Center, Moffett Field, CA 94035
 c Dept. of Aerospace Engineering, University of Illinois at Urbana-Champaign, IL 61801
 d Center for Hypersonics and Entry Systems Studies, University of Illinois at
 Urbana-Champaign, IL 61801
 e Dept. of Aeronautics and Astronautics, Stanford University, Stanford, CA 94305

11 Abstract

The diffusive tortuosity factor of a porous media quantifies the material's 12 resistance to diffusion, an important component of modeling flows in porous 13 structures at the macroscale. Advances in X-ray micro-computed tomogra-14 phy (μ-CT) imaging provide the geometry of the material at the microscale (microstructure) thus enabling direct numerical simulation (DNS) of trans-16 port at the microscale. The data from these DNS are then used to close ma-17 terial's macroscale transport models, which rely on effective material prop-18 erties. In this work, we present numerical methods suitable for large scale 19 simulations of diffusive transport through complex microstructures for the 20 full range of Knudsen regimes. These numerical methods include a finitevolume method for continuum conditions, a random walk method for all 22 regimes from continuum to rarefied, and the direct simulation Monte Carlo 23 method. We show that for particle methods, the surface representation sig-24 nificantly affects the accuracy of the simulation for high Knudsen numbers, 25 but not for continuum conditions. We discuss the upscaling of pore-resolved simulations to single species and multi-species volume-averaged models. Finally, diffusive tortuosities of a fibrous material are computed by applying 28 the discussed numerical methods to 3D images of the actual microstructure 29 obtained from X-ray computed micro-tomography. 30

1. Introduction

diffusion

31

32

Modeling flow in porous materials is of importance in many research areas, including porous thermal protection systems, energy storage systems,

Keywords: microtomography, tortuosity, microscale modeling, rarefied,

Email address: joseph.ferguson@stanford.edu (Joseph C. Ferguson)

Preprint submitted to Computational Materials Science

November 2, 2021

porous evaporators, filtration systems, to name a few. Deriving the governing equations of porous materials at the macroscale often relies on volume-averaged techniques, in which control volumes with effective material properties are treated as unit cells of the bulk material. The flow characteristics of a volume-averaged porous material are often defined by quantities related to the material micro-structure including the permeability and the diffusive tortuosity factor. The permeability of a material quantifies the wall drag resistance to a mean pressure gradient, while the tortuosity characterizes a material's effective resistance to diffusion.

The determination of effective transport properties in porous materials often relies on experimental methods. However, advances in computational methods enable predicting these properties numerically on realistic complex microstructures and non-trivial domain sizes [1–3]. These computational advances have been complemented by advances in X-ray microtomography, a technique that provides a high-resolution 3D representation of the actual microstructure of the material[1, 4]. Modern μ -CT technology can provide 3D-images with resolution from centimeter to micron scale. These images have become a powerful platform on which to numerically compute material properties [3, 5–7].

Before further discussing the diffusive tortuosity factor, it is worth noting that in the porous media literature, there are three distinct material properties that are described by the term tortuosity:

- 1. Hydraulic tortuosity: describes the length of flux streamlines compared to the straight-line path in a pressure driven flow [8, 9]. The value in this case is used to express the permeability in terms of parameters that reflect the geometry of porous materials [8].
- 2. Geometric tortuosity: ratio between the shortest path through a porous media and the straight-line path [10].
- 3. Diffusive/electrical/conductive tortuosity: impeding factor that quantifies a materials resistance to diffusion/conduction

Each of these definitions represent a distinct property (and concept) and cannot be used interchangeably. The distinctions and appropriate usage of each have been discussed in a number of review articles [11, 12] and in studies directly comparing the quantities [13]. In this paper, we focus exclusively on the diffusive tortuosity for gases. A simple model [14], inspired from the binary mixtures theory, is used as a first approximation to the apparent impeding diffusion in porous medium,

$$\langle \mathcal{F}^{\alpha} \rangle_{i} = \frac{\epsilon}{\eta_{ij}} D_{\text{ref}}^{\alpha} \frac{\partial \langle \phi^{\alpha} \rangle}{\partial x_{j}} = D_{\text{eff,ij}}^{\alpha} \frac{\partial \langle \phi^{\alpha} \rangle}{\partial x_{j}}$$
 (1)

where $\langle \mathcal{F}^{\alpha} \rangle_i$ is the apparent diffusion flux of species α in the *i*-direction due to macroscale gradient of the species in the *j*-direction (summation over *j*

is implied), ϵ is the porosity of the medium, η_{ij} the directional-tortuosity, D_{ref}^{α} is the reference diffusion coefficient of species α , $D_{\text{eff},ij}^{\alpha}$ is the reference anisotropic diffusion coefficient of species α . When modeling diffusion in porous media, the Knudsen number, typically defined as the ratio of the flow mean free path length to a selected length scale of the porous domain, must be considered in order to determine whether the continuum assumption is valid at the length scales of interest. Since micro-scale and volume-averaged modeling of porous materials have very different length scales, it is often the case that for a set of conditions, continuum modeling is appropriate at the macro-scale, but may be inappropriate for micro-scale (or pore-resolved) modeling.

Under continuum conditions at the micro-scale, classical numerical methods such as finite-difference, finite-volume, or finite-element can be used to solve the diffusion equation in the porous material. However, as the Knudsen number increases, the continuum equations are no longer valid for the physical system, for example in the case of high temperature, low pressure gases diffusing in fibrous media [15]. In such instances, particle methods such as random walks [16, 17] or the direct simulation Monte Carlo (DSMC) method [18] are used. For the purposes of this paper, we use Kn < 0.01 as continuum conditions, 0.01 < Kn < 0.1 as the slip regime, 0.1 < Kn < 10 as the transitional regime, and Kn > 10 as the rarefied regime [19].

At non-continuum conditions, the definition of tortuosity factor needs an associated length scale for reasons that will be described in Sec. 2. In most of the literature, the tortuosity factor has been defined as a function of the Knudsen number [15–17, 20, 21], while Zalc *et al.* [22] argues that this relationship only arises from an improper definition of the characteristic length scale.

In this paper, we discuss the physical model and numerical methods appropriate for the computation of the diffusive tortuosity factor of a porous material based on large X-ray micro-tomography images. In Sec. 2, we discuss a model that defines the tortuosity factor as a material property that exclusively depends on the geometry of its microstructure and is independent of the Knudsen number. Under this model, the non-continuum effects are captured in the definition of the length scale. Here, we also present the upscaling to macroscale simulations, including for multi-species diffusion. Sec. 3 presents the computational representation of materials in this study, with a focus on X-ray microtomography datasets. Sec. 4 presents the numerical methods used for solving diffusion in porous media, as well as the particular considerations necessary when computing the tortuosity factors in the three Knudsen regimes. Finally, in Sec. 5 we present direct comparisons between the numerical methods, and results for the tortuosity factors based on the X-ray microtomography of a highly porous carbon fiber material.

2. Physical Model

110

In this section, we present the physical model for the tortuosity factors and how to apply simulation results at the microscale to volume-averaged modeling tools. We begin with the definition of the tortuosity.

$$\eta = \epsilon \frac{D_{\text{ref}}}{D_{\text{eff}}} \tag{2}$$

where η is the tortuosity factor, D_{ref} is the reference diffusion coefficient, D_{eff} is the effective diffusion coefficient in the porous material, and ϵ is the porosity. Since the materials are not necessarily isotropic, we define the tortuosity in each direction using subscripts i and j. In the tortuosity tensor,

$$\eta_{ij} = \begin{bmatrix} \eta_{11} & \eta_{12} & \eta_{13} \\ \eta_{21} & \eta_{22} & \eta_{23} \\ \eta_{31} & \eta_{32} & \eta_{33} \end{bmatrix}$$
(3)

the diagonal terms are typically the most relevant, with very large off diagonal terms (meaning very high resistance to diffusion). An exception is for materials with anisotropic microstructures that are not aligned with the Cartesian axes.

2.1. Definition of the reference diffusion coefficient

119 Continuum regime

120

121

124

126

127

128

129

130

In the continuum regime, the reference diffusion coefficient can be simply defined as the single-species bulk diffusion coefficient [23]:

$$D_{\rm ref} = D_{\rm bulk} \approx \frac{1}{3} \bar{v} \bar{\lambda}$$
 (4)

where \bar{v} and $\bar{\lambda}$ are the mean thermal velocity and mean free path length of the gas particles, respectively.

Since both the mean thermal velocity and the mean free path are not directional, the reference diffusion coefficient in continuum conditions is also not directional.

Non-continuum regimes

In non-continuum regimes, however, the continuum regime definition of bulk diffusion begins to break down. The flow regime is quantified by the Knudsen number

$$Kn = \frac{\bar{\lambda}}{l_D} \tag{5}$$

where $l_{\rm D}$ is defined as the length scale of interest. In general, the length scale cannot be assumed equal in all directions; therefore, we denote the directional length scale as $l_{\rm D,i}$.

In the fully rarefied regime, $\lim_{K_{n}\to\infty} D_{\text{bulk}} = \infty$. However, the D_{eff} in Eq. 2 remains bounded, and plateaus for high Knudsen numbers. Thus, direct application of Eq. 2 for $D_{\text{ref}} = D_{\text{bulk}}$ would lead to a tortuosity that tends towards infinity with the Knudsen number.

It is therefore necessary to define a reference diffusion coefficient that remains bounded for free-molecular (Kn $\to \infty$) conditions. A common approach is to define $D_{\rm ref}$ as diffusion through a capillary of diameter $l_{\rm D}$. Using this definition, the continuum reference diffusion remains unchanged, since $D_{\rm ref} = D_{\rm bulk}$ for diffusion through the capillary. In the fully rarefied regime, the reference diffusion coefficient becomes $D_{\rm ref} = D_{\rm Kn} = \bar{v}l_{\rm D}/3$. As we will get to later, the choice of length scale can be a function of direction, so we define the fully rarefied reference diffusion coefficient as

$$D_{\text{ref,i}} = D_{\text{Kn,i}} = \frac{1}{3}\bar{v}l_{\text{D,i}}$$
 (6)

For Knudsen numbers that are outside of the fully continuum or fully rarefied regimes, (transitional or slip regimes), the Bosanquet approximation [24] is used to estimate a diffusion coefficient based on its bulk and Knudsen components [20], D_{bulk} and D_{Kn} , respectively.

$$\frac{1}{D_{\text{ref}}} = \frac{1}{D_{\text{bulk}}} + \frac{1}{D_{\text{Kn}}} \tag{7}$$

Applying the Bosanquet approximation to single-species diffusion in a capillary in direction i, $D_{\rm ref,i}$ is estimated to be

$$D_{\text{ref,i}} = \frac{1}{3}\bar{v} \left(\frac{\bar{\lambda}l_{\text{D,i}}}{\bar{\lambda} + l_{\text{D,i}}} \right) \tag{8}$$

The capillary model is convenient because the reference diffusion coefficient can be computed analytically from \bar{v} , $\bar{\lambda}$, and $l_{\rm D}$, and because $D_{\rm ref}$ converges to $D_{\rm bulk}$ at low Knudsen numbers and $D_{\rm Kn}$ at high Knudsen numbers. In later sections we show that this model for estimating transitional or slip regime diffusion coefficients based on the bulk and rarefied extremes works well even for complex 3D geometries.

2.2. Definition of the characteristic length

From the capillary model, a characteristic length scale of diffusion, $l_{\rm D}$, must be selected. In the surveyed literature related to diffusion in porous media, there have been a number of methods used to determine a characteristic length:

a. $l_{\rm D}$ is defined using an expression for estimating the mean pore diameter of a 3D media, such as $4\epsilon/S$ where ϵ is the porosity and S is the specific surface area. [15–17, 20, 21].

b. $l_{\rm D}$ is defined based on a numerical approximation for the mean pore diameter, such as the mean intercept length [25].

c. $l_{\rm D}$ is defined such that the tortuosity factor is the same for the continuum and rarefied extremes [22].

Assuming that the Bosanquet approximation is used to estimate transitional and slip regime diffusion coefficients, each of these methods require simulations to determine the effective diffusion coefficient at two different Knudsen numbers. Used properly, each method will also produce the same result when applying the computed tortuosity factors to determine an effective diffusion coefficient of a unit cell in a volume-averaged simulation. Comparing the options, the main difference lies in the definition of the tortuosity as a unique value or as a function of the Knudsen number.

An analysis of the three options led us to identify several advantages in using a definition of the tortuosity factor as a single geometry-dependent parameter [22], rather than as a function of the Knudsen number. One reason for this is simplicity: using the single value definition, given by length scale option (c), the tortuosity factor in a given direction is defined by two numbers, a single tortuosity factor value and a characteristic length. By contrast, in length scale options (a) and (b), the tortuosity factor in each direction is defined by three numbers, a bulk tortuosity factor, a Knudsen tortuosity factor, and a characteristic length. In addition, the definition of both a bulk and Knudsen tortuosity factor can arguably lead to confusion and misapplication, since the Knudsen tortuosity factor has no physical meaning without the characteristic length. Moreover, at certain conditions, some geometries yield unintuitive results of a tortuosity factor of less than one [17]. In summary, we chose length scale option (c), and we consistently do so in the remainder of this paper, unless explicitly specified.

Using length scale option (c), the length scale of diffusion is computed as

$$l_{\rm D,i} = \frac{3\eta_{\rm bulk} D_{\rm eff,Kn}^{\rm i}}{\epsilon \bar{v}} \tag{9}$$

where η_{bulk} is the bulk tortuosity factor computed using continuum assumptions, and $D_{\text{eff,Kn}}$ is the computed effective diffusion coefficient of the high Knudsen number simulation (see Sec. 4.2), and \bar{v} is the mean thermal velocity.

2.3. Applying the tortuosity factor for multi-species diffusion

Once the tortuosity factors and the length scale have been computed for a given microstructure (detailed in Sec. 4), they can be applied to compute the effective diffusion coefficient of a species in a material, in each of the three directions. In order to compute this value, one must first compute the bulk diffusion coefficient (not within the porous material) for species α

into the mixture, $D_{bulk}^{\alpha,m}$ at a given pressure and temperature, as well as the mean thermal velocity, \bar{v}^{α} . The reference diffusion coefficient for species α in the material, for a given direction i, is then computed as an algebraic manipulation of the Bosanquet approximation:

Once the reference diffusion coefficient is defined for a specific species and direction, the corresponding effective diffusion coefficient inside the porous material can be computed by as a manipulation of equation 2:

$$D_{\text{eff,i}}^{\alpha} = \frac{\epsilon}{\eta_i} \frac{D_{\text{ref,i}}^{\alpha,m}}{(11)}$$

This is most often used in the context of macro-scale modeling efforts [26], where diffusion is solved in a volume-averaged porous material. The presented model is valid for local thermal equilibrium applications. The application to local thermal non-equilibrium formulations, and possible correction terms to account for the thermal effects on diffusion, requires further study.

An example of a full workflow is presented in Appendix A1, which uses numerical methods presented later in this paper to calculate the tortuosity factors and length scales of a fibrous material. The effective diffusion coefficients for a Xenon-Argon mixture are then calculated using Eqs. 10 and 11 and compared to direct numerical simulation of the diffusion inside the porous media using Direct Simulation Monte Carlo.

3. Computational Representation of Arbitrary Porous Media

In this work, computational domains of porous media are either computationally generated using the Porous Microstructure Analysis (PuMA) software [27] or obtained from synchrotron X-ray micro-tomography. Synthetically (computationally) generated domains allow us to perform verification on simple structures, or perform analysis on structures with varying porosity, and to tailor certain features of interest such as fiber orientation, fiber diameter, etc., as well as to easily evaluate both fibrous structures and packed beds. On the other hand, computationally generated domains miss micro-scale features and variability of actual materials, which are captured by X-ray micro-tomography. The computational generation of simple materials is discussed in Appendix A2.

We store the material on a uniform 3D Cartesian grid, where each node, separated by unit length, is given a numerical value, as this is the typical format of microtomographic data. In a discrete representation, nodes are assigned a value of either 0 or 1, indicating whether the node is material or void. In a continuous representation instead, each node has a value within a

continuous range, and cutoff values are used to separate the material phases from one another. The 3D box defined by $\pm 1/2$ unit in each direction corresponds to a voxel. A physical length is ascribed to the voxel, called the voxel length. For typical micro-structural applications, this length may range between 10^{-7} and 10^{-4} meters.

For use in the particle simulations, discussed in Secs. 4.2 and 4.3, triangulation techniques, such as the marching cubes algorithm [28–30], can be used to approximate the interface between void and material as a collection of triangles. The marching cubes algorithm is well suited for simulations based on X-ray microtomography, since the iso-surface is triangulated directly on the 3D Cartesian grid. This triangulation can be performed on either a discrete or continuous grid. If performed on a discrete grid, triangles are limited to angles at 45° intervals, whereas on a continuous grid, triangles can be placed at any angle. This is visualized in Fig. 1, which shows a sphere of radius 6 voxels, visualized with a) no triangulation, b) with triangulation on a discrete grid, and c) with triangulation on a continuous grid.

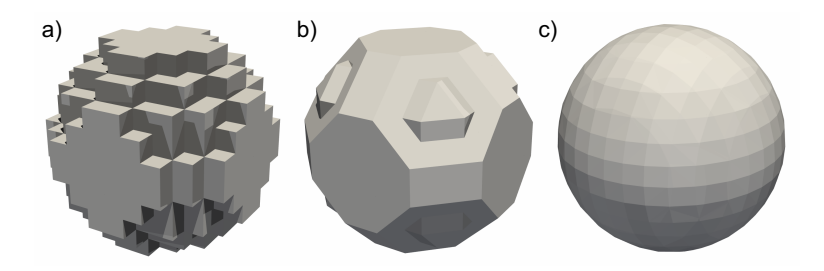


Figure 1: Visualization in ParaView [31] of a sphere of radius 6 voxels as an (a) voxel surface and (b) marching cubes triangulation on a discrete grid and (c) marching cubes triangulation on a continuous grid

Use of the original marching cubes algorithm results in an iso-surface that may not be water tight, as ambiguities in the algorithm can result in the formation of small holes. For particle-based simulations, this can result in particles entering and getting trapped in the solid material, potentially impacting the simulation results. This can be avoided by using modified marching cubes algorithms that guarantee a topologically correct surface [32, 33]. The marching cubes variant of Lewiner et al. is available in a number of free software packages, including PuMA [27] and scikit-image [34]

3.1. X-ray microtomography

X-ray microtomography measurements provide resolution of material structures at scales from micrometer to centimeter in a non-destructive fashion. The structure is resolved into a 3D voxelized grid where each voxel has a grayscale intensity proportional to the local X-ray attenuation.

The past two decades have witnessed a rapid development of computational methods and numerical tools based on 3D images. Applications to the direct computation of material properties have been demonstrated in structural analysis [35–37], prediction of thermal transport [38–42], and calculations of mass and momentum transport properties [43–46]. As applied to diffusive processes, Cooper et al. [47] and Tranter et al. [48] have developed tools for computations of tortuosity factors based on 3D images. Numerous applications exist in the field of woven materials [49], and many recent investigations have been dedicated to detailed tortuosity studies in electrochemistry [50, 51] and biology [52].

Today, X-ray micro-tomography is largely accessible through laboratoryscale scanners, which match synchrotron light sources in attainable spatial resolutions. Synchrotron tomography remains the primary choice for fast acquisition times and *in-situ* experimentation, providing wider flexibility in sample size, and experimental configurations. Our tomography work for this study was conducted at the beamline 8.3.2 of the Advanced Light Source at the Lawrence Berkeley National Lab [53, 54]. We used an X-ray energy of 14 keV to image a highly porous carbon fiber material called FiberForm, used as preform for lightweight ablative thermal protection systems [40]. For each scan we captured 1024 radiographs over a 180° arc, using a 10× magnification lens that provided a voxel size of $\approx 1.3 \mu m$. Because the material has variability in local porosity, density and fiber arrangement [40, 55, we collected a total of fifteen tomographic scans of the material from different regions of the same manufactured billet. In this work, we do not discuss large scale variabilities that the material features as a result of the manufacturing process.

Tomography datasets were reconstructed using TomoPy [56, 57], filtered and de-noised in fiji [58] when necessary and imported in PuMA as 8bit Tiff stacks. Because the acquired scans had satisfactory phase contrast, resulting in a distinct bi-modal grayscale distribution, a histogram shape-based segmentation was performed directly in PuMA to identify fibers and pore space. A visualization of the segmented tomography is shown in Fig. 2 for the FiberForm material. The smallest inset shows a high magnification of a fiber section, where the surface is triangulated using the marching cubes algorithm introduces in section 3.

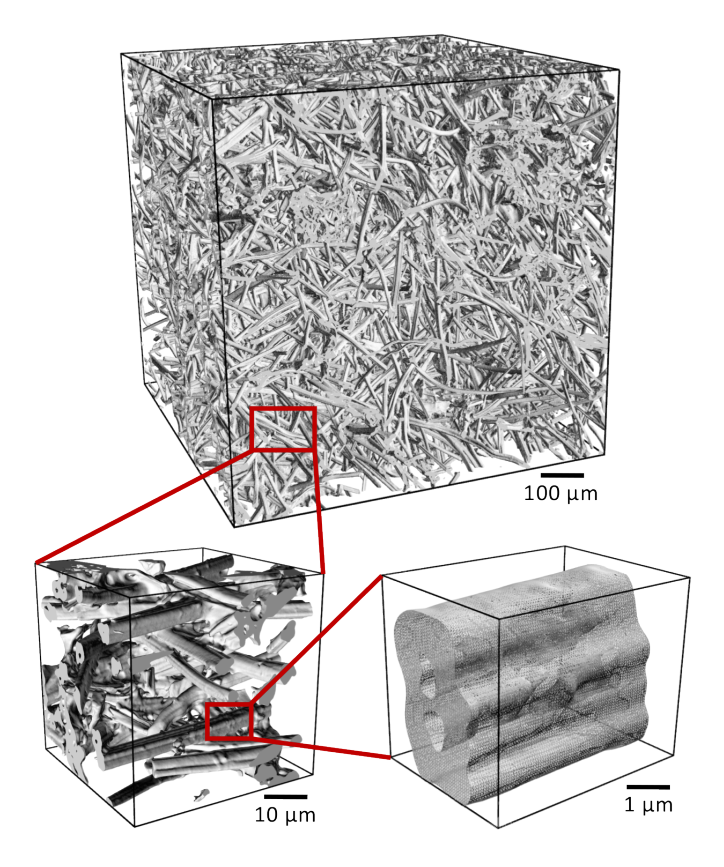


Figure 2: Surface rendering of 1 mm³ sample of FiberForm, taken at three resolutions and visualized in PuMA V2.1 [27].

4. Numerical Methods for Pore Resolved Diffusion Simulations

In this section, we present numerical methods suitable for direct numerical simulation of diffusive transport in porous media. While there are many numerical methods available, the presented numerical methods strike what we believe to be an appropriate balance between convenience and accuracy for large scale simulations based on X-ray microtomography images. In particular, the numerical method choices entirely avoid the generation of unstructured meshes, often a difficult and labor intensive process for complex microstructures.

4.1. Continuum methods

In the continuum, $\mathrm{Kn} < 0.01$ at the pore scale, typical numerical methods such as finite-difference, finite-volume, or finite-element can be used to determine the tortuosity factor of a porous material. From Eq. 2, we need

the porosity, ϵ , and the ratio of the reference and effective diffusion coefficients, $D_{\rm ref}/D_{\rm eff}$. To compute $D_{\rm eff}$ inside the porous material, the diffusion equation

$$\nabla \cdot (D_{\text{ref}} \nabla \phi) = 0 \tag{12}$$

is solved with an imposed concentration gradient at the boundaries in the direction of interest, where ϕ is the local concentration and $D_{\rm ref}$ is used as the local diffusion coefficient at all points in the void region. The result is the local concentration, ϕ at every cell in the computational domain, as shown in Fig. 3.

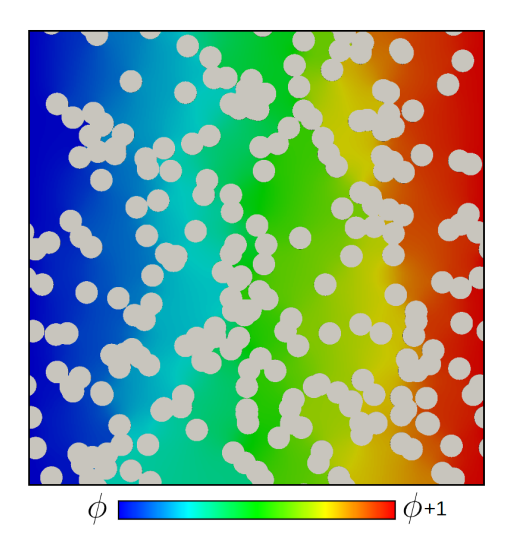


Figure 3: Steady state concentration profile for 2D diffusion through intersecting parallel cylinders. Simulation was run in the PuMA software on a carteesian grid [27, 59], and the visualization was generated in ParaView [31].

The average diffusive flux can then be determined, and used with Fick's first law of diffusion, $\mathcal{F} = -D_{\text{eff}} \nabla \langle \phi \rangle$, to compute the effective diffusion coefficient, where \mathcal{F} is the diffusive flux.

The tortuosity factor is then found in the direction of interest using Eq. 2. For the 3D tensor, a simulation must be run with imposed gradients in each of the three directions. For isotropic materials, three directions should yield approximately the same tortuosity factor.

In this work, a finite-volume solver implemented on a Cartesian grid was used. The finite-volume solver implements Dirichlet boundary conditions in the direction of interest and reflective boundary conditions in the side directions. The linear system is solved using the conjugate gradient method [60]. The solution is initialized with a linear concentration profile in the simulation direction. A residual tolerance of 10^{-4} is used. The conjugate gradient

solver typically convergences in a few thousand iterations for the fibrous microstructures of 800^3 voxels used in this study.

The solver was implemented into the Porous Microstructure Analysis (PuMA) software [27, 61] and parallelized using OpenMP [62].

The choice of solving the diffusion equation directly on a Cartesian grid, using a voxel representation of the surface, comes with significant computational advantages at the expense of a low order surface representation. A structured Cartesian grid allows large simulations to be performed, with domain sizes of 1000^3 elements or more on a large workstation. Alternatively, an unstructured mesh could be generated from the tomographic data with a higher order representation of the surface. Such an approach would pay a heavy cost both in terms of the generation of such meshes (often an arduous and manual process) and in computing the converged solution. The results shown in Fig. 7 and associated discussion provide an estimate to the error that can be expected for given feature sizes and porosities when computed on a voxel grid.

4.2. Random walk method

In non-continuum conditions, beginning around Kn > 0.01, the continuum equations presented in section 4.1 are no longer valid for the physical system. For simulations of single-spieces diffusion at all Knudsen regimes a random walk method has been implemented in PuMA [27] following past works of Tomadakis & Sotirchos [16, 17], Vignoles [20], and Becker et al. [63]. The random walk method simulates diffusion through the use of independently marching particles, that randomly move through the void space of a porous medium and collide with the pore walls. Particle-particle collisions are not directly simulated, but rather are assumed to occur once the particle has traveled a certain distance, based on the imposed mean free path length. For each simulation, the total number of particles, total walk time, mean thermal velocity, and mean free path length are imposed. The details of the random walk method are provided below, and available in the documentation of the PuMA source code [27].

Particle properties and placement

Particles are randomly placed in the pore space of the domain, and assigned a random unit direction vector. Each particle is given the same thermal velocity, input for the simulation. A random free path length is assigned to each particle, based on an exponential distribution:

$$\lambda = -\log(R)\bar{\lambda} \tag{13}$$

where R is a uniform random number, $R \in (0,1)$, and $\bar{\lambda}$ is the mean free path length, imposed for the simulation.

Particle movement

As each particle moves through a voxel, one of the following three conditions occurs (see Fig. 4): (a) the particle continues to the next voxel intersection, (b) the walk distance exceeds the free path length of the particle, or (c) a collision occurs with the material.

In case (a), the particle continues to the next voxel. In case (b), a particle-particle collision is simulated (though no actual collision occurred since the particles walk independently). A new random unit direction vector is given to the particle, and a new free path length is picked from the exponential distribution in Eq. 13. In case (c), a particle-surface collision occurs, and the particle is given a new direction vector based on a diffuse reflection with the surface. The particle is also given a new free path length from the exponential distribution in Eq. 13.

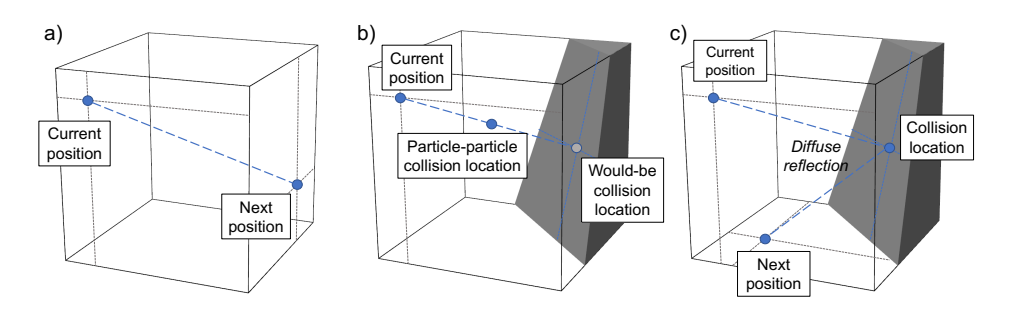


Figure 4: Schematic of random walk particle traversing a voxel, showing the three possible cases: (a) no collision, (b) particle-particle collision, (c) particle-wall collision.

Surface collision detection

Particle-surface collisions were tested based on two surface representations, a voxel grid and an iso-surface approximation based on marching cubes. In section 3 we discuss the use of the two methods in determining surface collisions and scattering when simulating diffusion.

Boundary conditions

Reflective (symmetric) boundary conditions are used for the computational domain. In our implementation, the particles are not bounded to the domain, but rather the domain is infinitely reflected and every possible voxel is associated with a specific voxel in the domain, as shown in Fig. 5. If the number of reflections is odd, the triangles contained in the voxel must also be reflected. The choice of reflective rather than periodic boundary conditions was made in order to preserve the average tortuosity at the boundary. If periodic boundary conditions are used on a non periodic material, then at the boundary the diffusion is impeded by the extra material reflected from the opposite side of the domain, with an effect size inversely proportional to the material porosity.

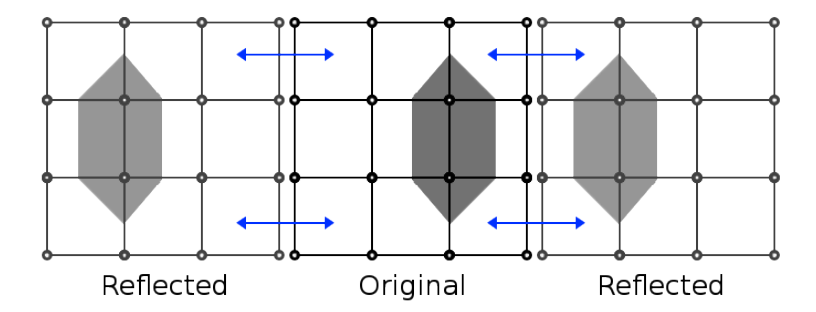


Figure 5: 2D Visualization of reflective boundary condition used for the random walk diffusion solver

Determination of the effective diffusion coefficient 404

Once the simulation has converged, the effective diffusion coefficient, in direction i, is determined as [64]

$$D_{\text{eff,i}} = \frac{\langle \xi^2 \rangle_i}{2t} \tag{14}$$

where $\langle \xi^2 \rangle_i$ is the mean square displacement of the particles in the direction i, and t is the simulation time. In the typical process for determining the 408 tortuosity factor, described in section 2, the computed value for D_{eff} , and 409 the mean free path length, λ would be used in Eq. 9 to determine the 410 characteristic length of diffusion.

Parallelization of the algorithm

405

406

411

412

413

414

415

416

417

418

419

420

421

422

423

424

425

426

427

428

429

Because the walkers operate independently, the algorithm is easily parallelized for shared memory or distributed memory systems. Our OpenMP [62] parallelization scheme, which simply uses a parallel for-loop over the particles, obtains near perfect scaling when tested on a 44-core machine with approximately 2300 particles per processor.

Computing the tortuosity factors from random walk simulations

Assuming the use of Bosanquet's approximation to estimate the transitional and slip regime diffusion coefficients, the diffusive tortuosity factors of a material are defined in each relevant direction by the tortuosity factor, η , and the length scale of diffusion, $l_{\rm D}$. Using the random walk solver, they are computed as follows:

- 1. Select a mean free path length and mean thermal velocity in continuum conditions, and compute D_{ref} using Eq. 4.
- 2. Using the selected conditions, run a continuum random walk simulation to determine D_{eff} in a material.
- 3. Use $D_{\rm eff}$ and $D_{\rm ref}$ from steps 1 & 2 to compute the tortuosity factor, η , from Eq. 2.

- 4. Select a new mean free path length in the transitional/rarefied regime. Using these conditions, run a random walk simulation and compute $D_{\rm eff}$ inside the porous material.
- 5. Use Eq. 9 with the transitional/rarefied conditions to compute $l_{\rm D}$.

4.3. Direct Simulation Monte Carlo

 Although the random walk method detailed above is capable of solving for the tortuosity factors and length scales, simulations using Direct Simulation Monte Carlo (DSMC) were also conducted. The DSMC simulations were used as a verification tool for the random walk algorithm, and to perform direct numerical simulation of multi-species diffusion in porous media to compare with our presented model (see Appendix A2). In a typical workflow, however, the computational expense of DSMC simulations, particularly in the continuum regime, make DSMC an impractical choice.

DSMC is a stochastic method that solves the time-dependent nonlinear Boltzmann equation. It is a probabilistic simulation of molecular processes based on the kinetic theory of dilute gases [18]. DSMC is often used for the simulations of fluid flows in non-continuum conditions; though valid in the continuum regime, the high particle density requires at this regime results in high computational cost. In the DSMC algorithm, the Boltzmann equation is decoupled into two parts: molecular advection and collisions.

Particles are tracked in the domain based on their position in virtual cells. Each particle represents an F_N number of real molecules. The cell length has to be carefully chosen such that it is smaller than the mean free path length. The time step is chosen such that it is smaller than the mean collision frequency. At each time step, following their advection, a number of binary pairs of particles are selected for collisions in each grid cell. In the collision procedure, we follow the no-time-counter (NTC) procedure of Bird [18] for the selection of collision pairs. Quantities such as velocity, translational and internal energy of particles can be computed by sampling the flow field. Therefore, macroparameters such as temperature, pressure and number density can be computed in each grid cell. In order to reduce statistical scatter and ensure that collisions are performed accurately, it is generally recommended that a minimum of 10 to 20 particles per computational cell be used [65].

The Stochastic PArallel Rarefied-gas Time-accurate Analyzer (SPARTA) [66, 67] DSMC code developed at Sandia National Laboratories was used in the current work. The grid was used to group particles by grid cell for purposes of performing collisions and chemistry, as well as efficiently find particle/surface collisions. As in the random walk solver, the marching cubes algorithm [28, 29] was also implemented in SPARTA [45] to approximate the iso-surface of the digitized geometry from either micro-tomography or artificially generated, given a grayscale threshold. The algorithm represents the surface of the fibers as a collection of triangles. These were used to locate surface collisions with particles during the DSMC simulation.

Argon was initially chosen as the carrier gas. SPARTA uses the Variable Hard Sphere (VHS) model to simulate particle interactions [18]. The particle-surface collisions were modeled using a diffuse reflection model.

477 Computing the tortuosity factors from DSMC simulations

From the quantities computed in a DSMC simulation, the tortuosity factor of a material is computed as follows:

- 1. Perform DSMC simulations in a periodic box with no surface elements to compute the bulk diffusion coefficient D_{bulk} for the simulation ¹.
- 2. Run a free molecular simulation (inter-particle collisions turned off) to determine $D_{\rm eff,Kn}$ in a material.
- 3. Run a simulation in the continuum or slip/transitional regime 2 , and compute D_{eff} inside the porous material using Eq. 14.
 - 4. Compute η from $\eta = D_{\text{bulk}} \cdot (1/D_{\text{eff}} 1/D_{\text{eff,Kn}})$.
- 5. Compute l_D from Eq. 9 with $1/\lambda = 0$.

480

481

486

490

491

492

493

494

495

496

497

498

499

500

501

502

503

488 5. Application of Numerical Methods

489 5.1. Consideration 1: Surface Representation

For each of the numerical techniques used to simulate diffusion in porous media, a method was needed to represent the boundary between void and material. For particle simulations, the surface can be represented as either a voxel grid, as shown in Fig.1a, or as a triangulated iso-surface, as shown in Fig.1b and c.

A study was performed to assess how the collision detection based on the two surface discretizations affects the computed effective diffusion coefficient. Figure 6 shows the percent difference between effective diffusion coefficient D_{eff}^{vox} and D_{eff}^{iso} computed on the voxel grid and the triangulated iso-surface of a continuous grid for Knudsen numbers from the continuum to the rarefied regime. In the continuum regime, where the mean free path length is small compared to the characteristic length of the geometry, the two collision methods yield results within 1% of each other. However, significant differences are noted at high Knudsen numbers. This effect exists

¹simulations were performed for argon at 273.15 K and various pressures and confirmed that all computed quantities are within 2% of the value of the diffusion coefficient calculated from the Chapman-Enskog first order approximation[18, 68]

²Although a continuum simulation in step 3 would produce the most accurate results, such simulations may not be feasible depending on the domain size and computational resources available.

independently of grid refinement and is due to an increased number of surface collisions that occur on a voxel grid. Take, for example, free molecular simulations 3 on the geometries shown in Fig. 1a and c, in which particles are randomly placed in the domain, directed towards the sphere. With the triangulated iso-surface, as shown in Fig. 1c, each particle will collide with the geometry exactly once before exiting the domain. However, for the voxel representation (Fig. 1a), our simulations showed that each particle collided with the surface an average of ≈ 1.54 times. This result was consistent for all domain and sphere sizes tested.

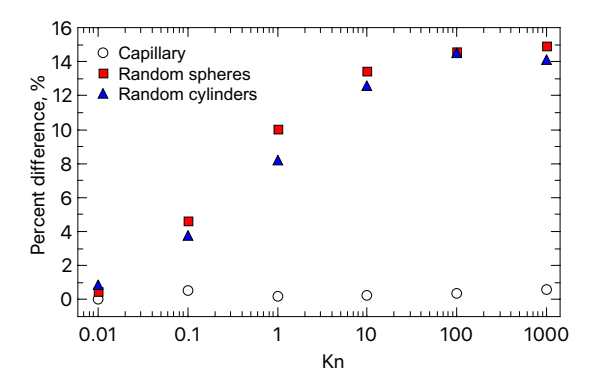


Figure 6: Percent difference in effective diffusion coefficient between simulations using a voxel or iso-surface collision method. Results are shown for a 1D capillary, a 3D random intersecting packed sphere bed, and 3D random intersecting isotropic fibers.

A similar effect was noted by Vignoles [20], where differences were studied in the computed mean intercept length, \bar{d} , in a cylindrical capillary using a voxel surface or a triangulation based on a discrete grid (rather than a continuous grid). Vignoles showed that for a triangulated surface, the mean intercept length converged to reasonable agreement with the physical diameter of the capillary. However, for a voxel surface representation, the mean intercept length was underestimated by around 20%. Simulations in PuMA corroborate these results.

As shown in Fig. 6, though the surface representation in the case of 1D diffusion in a capillary will affect the computed mean intercept length, it does not affect the value for the effective diffusion coefficient. This is explained by the fact that, for a cylindrical capillary, regardless of whether a voxel or triangulated surface is used, the surface normals will always be orthogonal to the capillary direction. For simulations in a capillary, using

³In a free molecular simulation, there are no particle-particle collisions, and each particle travels on an uninterrupted trajectory between particle-surface collisions.

the mean intercept length to define the characteristic length, as is the case with length scale option (b) (cf. Sec. 2.2) this result will have an effect on the computed tortuosity factor in the Knudsen regime, proportional to the difference in computed mean intercept length. The net effect, however, for the specific case of simulating diffusion in a capillary, is that both the voxel and triangulated surfaces yield good results for computing the effective diffusion coefficient and tortuosity factors, so long as the length scale method chosen is applied consistently.

For complex 3D structures, as shown in Fig. 6, the effect of using a voxel surface representation exists both for calculations of the mean intercept length and the effective diffusion coefficient, demonstrating that the differences between surface representation methods are significant and cannot be ignored.

As the iso-surface is a higher-fidelity representation of the real surface at the scale considered, we interpret this to suggest that a voxel surface is not adequate for simulations in the transitional and rarefied regimes. It is noted, however, that for simulations on actual materials, the iso-surface representation smooths effects that are due to roughness scales below the resolution of the imaging technique.

5.2. Consideration 2: Feature Resolution

For each of our numerical methods, the accuracy of the solution will depend on the discretization size. This effect is most significant in the case of voxelized surface representation, as used in the finite volume method, and the random walk with voxel surfaces. A parametric study was conducted on the random sphere and cylinder structures to estimate the error introduced by under-resolved features. Figure 7 presents results from the tortuosity computations on a 1024^3 grid (chosen large enough to be a representative volume) with shape primitives of varying radii at four porosity values. An approximate converged value for the tortuosity, η^* , was defined as an average of the tortuosity values for the four largest radii. As expected, the tortuosity value converges as the radius of the primitive shape increases. The convergence is also strongly related to the porosity, indicating that the mean pore diameter is a relevant factor.

Based on this parametric study, for the comparison between the random walk and finite-volume methods, for the comparison between numerical methods, presented in Sec. 6, radius values of 32 and 28 voxels were taken for the sphere and cylinder primitives, respectively. Since the random walk algorithm determines particle-surface collisions based on a marching cubes triangulation, it is an immersed boundary rather than a voxel-based solver. Thus, the solution converges at much smaller primitive shape radii values.

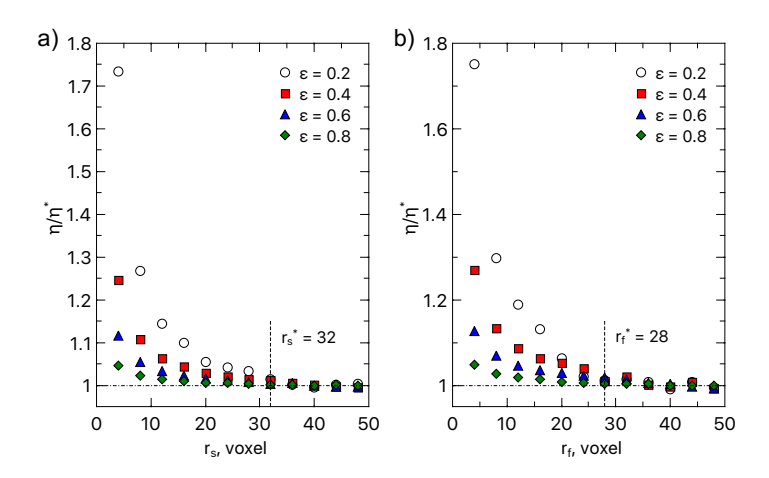


Figure 7: The convergence of tortuosity values as a function of shape primitive radius size for (a) packed sphere beds, and (b) random fiber structures, presented at four porosity values.

5.3. Consideration 3: Representative Elementary Volume

Another important parameter is the representative elementary volume (REV) at the selected resolution values. The REV defines the size at which the domain becomes statistically representative. The size of the REV varies for the property of interest [27], and is strongly dependent on the particular material. As such, the REV of artificially generated fibrous materials should not be extrapolated to that of real fibrous materials.

For our artificially generated materials, Fig. 8 shows the standard deviation of tortuosity values as a function of domain size for the random sphere and cylinder structures. The primitive shape radii were set to be 32 and 28 voxels, for the spheres and cylinders, respectively, and an additional parametric analysis was run at four porosity values.

Based on the results shown in Fig 8, a domain size of 1024^3 voxels was selected for the comparison between the finite-volume and random walk methods, presented in Sec. 6, such that the relative standard deviation would remain below 2% for both structures.

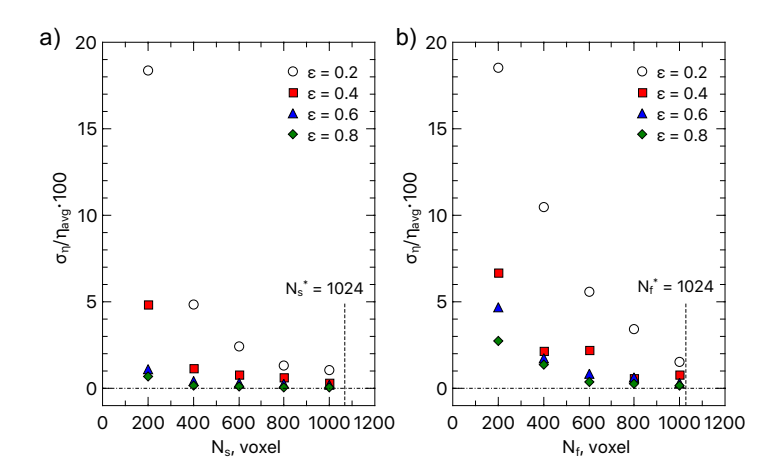


Figure 8: Relative standard deviation for (a) packed sphere beds and (b) randomly oriented fibers at varying domain sizes and porosities.

583 6. Direct Comparison of Numerical Methods

6.1. Continuum Tortuosity Factors

Figure 9 shows comparison between random walk and finite-volume methods, simulated on 3D fiber structures and a packed sphere beds of varying porosities. For continuum conditions, DSMC becomes prohibitively expensive. As such, DSMC results are not presented in this section. The random walk simulations were performed with 100,000 particles for a total walk length of 1000 times the domain size. A mean free path length of 0.5 voxels was chosen, ensuring the simulation occurs in the continuum regime. Simulations were performed on a 44-core (two Intel Xeon E5-2699 v4 processors) workstation, with simulation times of approximately 20 minutes each for both random walk and finite-volume simulations. The finite-volume and random walk simulations required approximately 50gb and 20gb of ram, respectively, for an 800³ domain size.

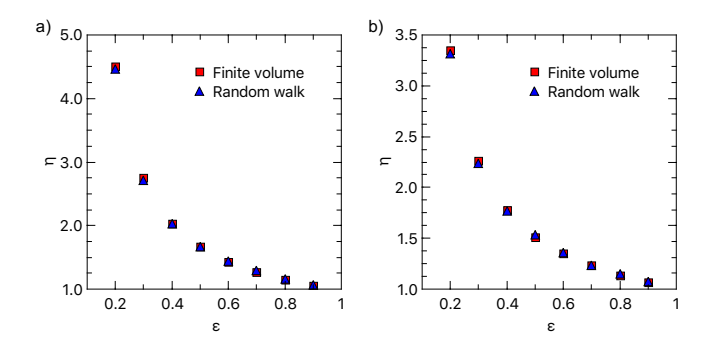


Figure 9: Comparison in computed tortuosity factors for (a) packed sphere beds and (b) randomly oriented 3D fibers, computed at multiple porosity values.

As shown in Fig. 9, the random walk and finite-volume methods showed excellent agreement for each material tested at all porosity values, with an average percent difference of 0.9% and a maximum percent difference of 1.7% between the two methods. As detailed in Sec. 5.1, in continuum conditions the choice of the surface representation for the random walk method becomes negligible. These results demonstrate the ability of the random walk method to accurately compute diffusion in the continuum regime on arbitrary 3D geometries.

6.2. Non-continuum Tortuosity Factors

In this section we compute diffusion coefficients and tortuosity factors at Knudsen numbers above 0.01. Random Walk simulation results are compared to the solutions obtained from DSMC, which is considered the accurate standard for computing transport in the transitional and rarefied flows.

Effective diffusion coefficients were computed with DSMC at discrete values of the Knudsen number. To this end, we fixed the gas and surface temperatures at 273.15 K for all cases (we start from a thermal equilibrium), and set the average pressures in the sample such that the mean free path length would be at least twice the cell size. The time step was chosen as 1 ns for all simulations, ensuring that it was at most 1/10 of the mean collision time. At least 12 particles were present on average in each cell of the domain for all simulations, in order to reduce statistical scatter. For the presented cases, this resulted in between 65 and 410 million particles for each simulation. The simulation was allowed to reach steady state for 5,000 timesteps, followed by an additional 40,000 timesteps for computation of the effective diffusion coefficient. A gas phase collision free molecular simulation was also performed in order to compute the exact value of $D_{\rm eff,Kn}$.

Simulations were performed on 1,200 Intel Haswell cores of the NASA Ames' Pleiades supercomputer, and the total simulations length varied be-

tween 30 minutes and 2 hours depending on the Knudsen number and geometry considered.

For the random walk results presented, 100,000 particles were used for a total walk length of 1000 times the domain length to ensure convergence. The mean free path length was adjusted to vary the Knudsen number of the simulation. As detailed in Sec. 5.1, triangulated surfaces are used for all simulations in non-continuum conditions. Simulations were performed on a 44-core workstation, with simulation times between 2 minutes and 20 minutes each depending on the Knudsen number.

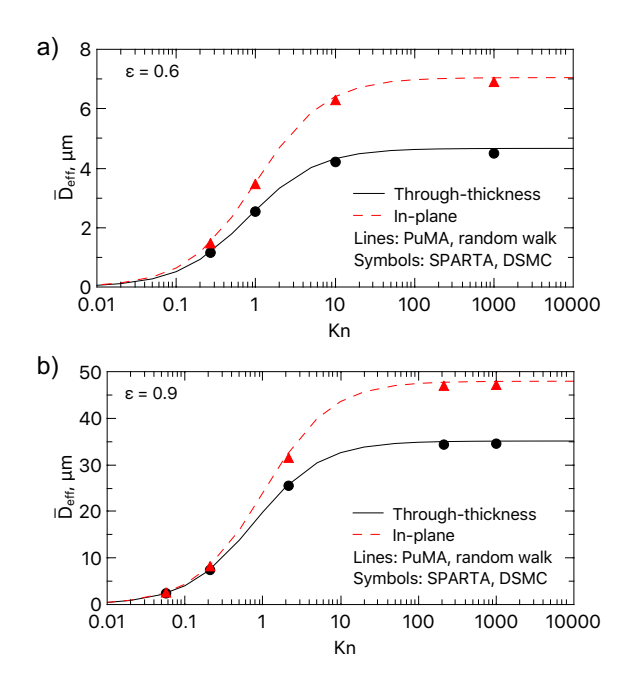


Figure 10: DSMC and random walk comparison in normalized effective diffusion coefficient as a function of Knudsen Number for randomly oriented transverse isotropic 3D cylinders at a) 0.6 and b) 0.9 porosity.

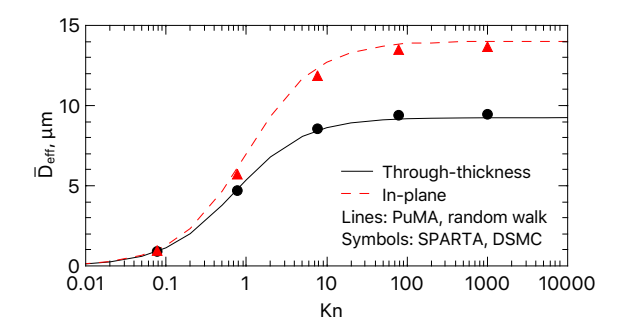


Figure 11: DSMC and random walk comparison in normalized effective diffusion coefficient as a function of Knudsen Number, computed on an X-ray microtomography image of FiberForm with side length 0.5mm and a porosity of 0.846.

Figure 10 shows the normalized effective diffusion coefficient, $\bar{D}_{\rm eff} =$ $D_{\rm eff}/\bar{v}$, computed on transverse isotropic random 3D fiber structures, with \pm 15 degree pitch with respect to the through thickness plane, at two porosity values (0.6 and 0.9) and at Knudsen numbers varying between 0.01 and 10,000. For the random walk simulations, the mean thermal velocity, \bar{v} is a simulation input; for the DSMC simulations, \bar{v} is a function of the input system temperature and gas species. The Bosanquet approximation for the slip and transitional regimes are plotted, based on Eq. 10, for the PuMA simulation results. Figure 11 shows the comparison on X-ray microtomography image of FiberForm, with 0.5mm side lengths, 400^3 voxels, and a porosity of 0.846., see Fig. 2. Note that given the inhomogeneity of FiberForm, this is not a sufficient size to be a representative volume. The size was limited because of the high computational cost of DSMC simulations, however it still serves as a good case for comparison between the numerical methods. It can be seen that the random walk and DSMC results show excellent agreement for complex 3D geometries at all Knudsen numbers.

6.3. Comparison with literature

635

636

637

638

639

640

641

642

643

644

645

646

647

648

649

650

651

652

653

654

655

656

657

658

Simulations using the random walk and DSMC methods were compared to results from the classical work of Tomadakis and Sotirchos [17] on 1D and 3D fiber structures. Tomadakis and Sotirchos used a tortuosity factor nomenclature which defines the characteristic length as an approximation of the mean pore diameter, $l_{\rm D}=4\epsilon\cdot S$. As explained in section 2, in this formulation, the tortuosity factor becomes a function of the Knudsen number. For this comparison, we have adopted their formulation. Results are presented in Figs. 12 and 13, for 1D and 3D fiber structures, respectively.

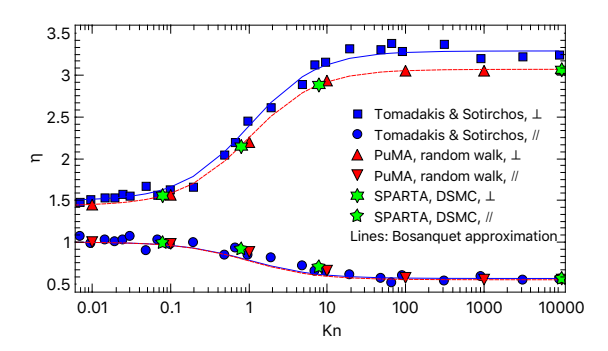


Figure 12: Simulation results from random walk and DSMC solvers on a 1D fiber structure with a porosity of 0.7 compared to results from Tomadakis and Sotirchos [17].

The dashed lines show the approximation of the tortuosity factor values in the slip and transitional regimes, given by

$$\eta = \frac{\eta_b + \eta_{\rm Kn} \cdot {\rm Kn}}{1 + {\rm Kn}} \tag{15}$$

where η_b is the bulk tortuosity factor as $\mathrm{Kn} \to 0$ and η_{Kn} is the rarefied tortuosity factor as $\mathrm{Kn} \to \infty$. While the random walk and DSMC results show excellent agreement, small differences exist in comparison to the Tomadakis and Sotirchos results. Statistical fluctuations, owing to the computational limitations in 1993 could account for the differences, as the simulations of Tomadakis and Sotirchos were performed with only 200 particles.

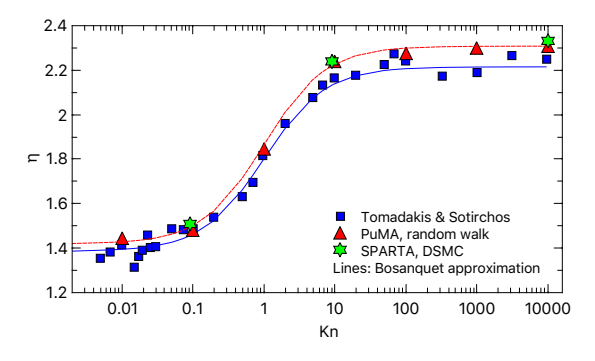


Figure 13: Simulation results from random walk and DSMC solvers on a 3D fiber structure with a porosity of 0.6 compared to results from Tomadakis and Sotirchos [17].

Another possible source of error is the geometry itself, as slight differences in geometry generation techniques could alter the results. This is supported by the similarity in results on 1D fibers in the parallel direc-

tion, which should be independent of the cylinder placement as long as the porosity and surface area are consistent.

6.4. Application to X-ray microtomography

Simulations were performed to determine the tortuosity factors of a material, FiberForm, based on X-ray microtomography images. Results from sections 4.1 - 6.3 demonstrated that the results of the random walk are consistent with other numerical methods at all Knudsen numbers. Therefore, the random walk methods is used, following the procedure in section 4.2 to compute the tortuosity factors of the material.

Fifteen different X-ray microtomography datasets of FiberForm were used, each of side length $1.04\,\mathrm{mm}$, with 800^3 voxels of length $1.3~\mathrm{\mu m}$. The datasets were each acquired as described in section 3.1 and down sampled by a factor of 2. In order to reduce noise and improve segmentation a bilateral filter with a radius of 3 and a range of 50 was applied to each image using Fiji [69], along with a despeckle operation. The X-ray microtomography datasets had a mean porosity of 0.887 with a standard deviation of 0.007.

For each tomography, a continuum simulation was carried out to compute the bulk tortuosity factor and a high-Knudsen number simulation was performed to determine the characteristic length of diffusion, $l_{\rm D}$. All simulations used 100,000 particles and a 1000 times the domain length total walk path; continuum simulations were given a mean free path length of 0.5 m, while rarefied simulations were given a mean free path length of 0.5 m.

As FiberForm is a transverse isotropic material [40], simulations were performed for both the "through-thickness" (z) and "in-plane" (x-y) direction. Results are shown for each of the 15 FiberForm samples in table 1, with averages and standard deviations shown.

Sample	Porosity	η_{IP}	η_{TT}	$l_{D_{IP}}$	$l_{D_{TT}}$
1	0.893	1.158	1.257	7.509e - 5	5.267e - 5
2	0.884	1.173	1.354	$7.946e{-5}$	$4.341e{-5}$
3	0.901	1.137	1.223	$8.623e{-5}$	$6.128e{-5}$
4	0.884	1.173	1.312	$7.146e{-5}$	$4.853e{-5}$
5	0.877	1.195	1.355	$6.632e{-5}$	$4.366e{-5}$
6	0.883	1.165	1.302	7.090e - 5	$4.965e{-5}$
7	0.885	1.175	1.326	$7.390e{-5}$	$4.751e{-5}$
8	0.888	1.162	1.299	$7.624e{-5}$	$5.170e{-5}$
9	0.881	1.178	1.339	$6.938e{-5}$	$4.434e{-5}$
10	0.883	1.171	1.335	$7.355e{-5}$	$4.514e{-5}$
11	0.890	1.155	1.277	$8.089e{-5}$	$5.299e{-5}$
12	0.876	1.186	1.357	$6.455e{-5}$	$4.251e{-5}$
13	0.894	1.164	1.220	7.673e - 5	$6.251e{-5}$
14	0.895	1.137	1.242	$8.517e{-5}$	$5.745e{-5}$
15	0.892	1.141	1.241	$8.795e{-5}$	$5.520e{-5}$
Average	0.887	1.165	1.296	7.585e - 5	5.5056e - 5
Std. Deviation	0.007	0.017	0.049	7.042e - 6	6.470e - 6

Table 1: Diffusive tortuosity factors of FiberForm, computed in the through-thickness and in-plane directions, for 15 X-ray microtomography scans.

These results show the expected difference in tortuosity factors in the through thickness and in plane directions. They also show that the relative standard deviation between samples is significantly higher for simulations of rarefied diffusion than in continuum diffusion, as seen by the larger relative standard deviations in the characteristic length than in the tortuosity factors.

7. Conclusions

 A physical model for the diffusive tortuosity factors is presented, in which the tortuosity factors of a material are independent of the Knudsen number. The random walk model is tested against a finite-volume method in the continuum regime, showing excellent agreement for simple and complex geometries at multiple porosities. It was shown that for low-resolution material domains, the voxel-based finite-volume method produces significant error at low porosity values, and a more refined voxel grid must be used. It was also shown that in the transitional and rarefied regimes, there are large differences in simulations on triangulated iso-surfaces and voxel grids, regardless of domain size. We interpret these differences to indicate that for particle-surface collision detection and reflections at high Knudsen numbers, an iso-surface representation should be used, although this claim

needs experimental validation. A DSMC solver was used to compute tortu-717 osity factors in non-continuum conditions. DSMC results were compared to 718 the random walk solver results, showing excellent agreement at all Knudsen numbers. The comparisons with the finite-volume and DSMC solvers 720 show that the random walk method is suitable for computing the diffu-721 sive tortuosity factors of an arbitrary 3D porous material at all Knudsen 722 numbers. Finally, the random walk method is applied to X-ray microto-723 mography datasets in order to compute the tortuosity of fibrous materials 724 used for spacecraft heatshields. 725

726 Acknowledgements

This research was supported by the NASA Entry System Modeling project. 727 Part of this work was also supported by the NASA Space Technology Re-728 search Fellowship program (Ferguson) under award No. 80NSSC19K1134, 729 and the Air Force Office of Scientific Research Young Investigator Program 730 (Panerai) under grant number FA9550-19-1-0050. This research used re-731 sources of the Advanced Light Source, a U.S. DOE Office of Science User 732 Facility under contract no. DE-AC02-05CH11231. The authors would also 733 like to thank F. Semeraro and J. Thornton for their contributions to the PuMA software. J. Haskins and K. Swaminathan-Gopalan are also acknowl-735 edged for their review of the manuscript and useful feedback. 736

737 Data Availability

The raw data required to reproduce the full example shown in Appendix
Al are available to download from the supplemental materials of this article. The 15 raw tomographic datasets of FiberForm are available from the
authors upon request.

742 References

743 References

- [1] E. Maire, X-ray tomography applied to the characterization of highly
 porous materials, Annual Review of Materials Research 42 (2012) 163–
 178.
- [2] B. L. Trembacki, D. R. Noble, M. E. Ferraro, S. A. Roberts, Mesoscale effects of composition and calendering in lithium-ion battery composite electrodes, Journal of Electrochemical Energy Conversion and Storage 17 (4) (2020).

- [3] M. C. Krygier, T. LaBonte, C. Martinez, C. Norris, K. Sharma, L. N.
 Collins, P. P. Mukherjee, S. A. Roberts, Quantifying the unknown impact of segmentation uncertainty on image-based simulations, Nature communications 12 (1) (2021) 1–11.
- J. Hsieh, Computed tomography: principles, design, artifacts, and recent advances, Vol. 114, SPIE press, 2003.
- [5] C. H. Arns, M. A. Knackstedt, M. V. Pinczewski, W. Lindquist, Accurate estimation of transport properties from microtomographic images,
 Geophysical research letters 28 (17) (2001) 3361–3364.
- [6] E. Maire, J.-Y. Buffiere, L. Salvo, J. J. Blandin, W. Ludwig, J. Letang,
 On the application of X-ray microtomography in the field of materials
 science, Advanced Engineering Materials 3 (8) (2001) 539–546.
- [7] L. N. Collins, S. A. Roberts, Mesoscale simulation of woven composite design decisions, arXiv preprint arXiv:2104.13554 (2021).
- [8] A. Duda, Z. Koza, M. Matyka, Hydraulic tortuosity in arbitrary porous
 media flow, Physical Review E 84 (3) (2011) 036319.
- [9] X. Zhang, M. A. Knackstedt, Direct simulation of electrical and hydraulic tortuosity in porous solids, Geophysical research letters 22 (17) (1995) 2333–2336.
- ₇₇₀ [10] P. Adler, Porous media: geometry and transports, Elsevier, 2013.
- 771 [11] M. B. Clennell, Tortuosity: a guide through the maze, Geological Society, London, Special Publications 122 (1) (1997) 299–344.
- ⁷⁷³ [12] B. Ghanbarian, A. G. Hunt, R. P. Ewing, M. Sahimi, Tortuosity in porous media: a critical review, Soil science society of America journal ⁷⁷⁵ 77 (5) (2013) 1461–1477.
- H. Saomoto, J. Katagiri, Direct comparison of hydraulic tortuosity and electric tortuosity based on finite element analysis, Theoretical and Applied Mechanics Letters 5 (5) (2015) 177–180.
- 779 [14] M. M. Tomadakis, S. V. Sotirchos, Ordinary, transition, and knudsen 780 regime diffusion in random capillary structures, Chemical engineering 781 science 48 (19) (1993) 3323–3333.
- [15] J. Lachaud, I. Cozmuta, N. N. Mansour, Multiscale approach to ablation modeling of phenolic impregnated carbon ablators, Journal of
 Spacecraft and Rockets 47 (6) (2010) 910.

- [16] M. M. Tomadakis, S. V. Sotirchos, Knudsen diffusivities and properties
 of structures of unidirectional fibers, Aiche journal 37 (8) (1991) 1175–
 1186.
- ⁷⁸⁸ [17] M. M. Tomadakis, S. V. Sotirchos, Ordinary and transition regime diffusion in random fiber structures, AIChE Journal 39 (3) (1993) 397–412.
- [18] G. A. Bird, Molecular gas dynamics and the direct simulation of gas
 flows, Clarendon, 1994.
- [19] G. Karniadakis, A. Beskok, N. Aluru, Microflows and nanoflows: fundamentals and simulation, Vol. 29, Springer Science & Business Media,
 2006.
- [20] G. Vignoles, Modelling binary, knudsen and transition regime diffusion
 inside complex porous media, Le Journal de Physique IV 5 (C5) (1995)
 C5-159.
- [21] G. L. Vignoles, O. Coindreau, A. Ahmadi, D. Bernard, Assessment
 of geometrical and transport properties of a fibrous C/C composite
 preform as digitized by X-ray computerized microtomography: Part II.
 Heat and gas transport properties, Journal of materials research 22 (6)
 (2007) 1537–1550.
- J. M. Zalc, S. C. Reyes, E. Iglesia, The effects of diffusion mechanism
 and void structure on transport rates and tortuosity factors in complex
 porous structures, Chemical Engineering Science 59 (14) (2004) 2947–
 2960.
- [23] W. G. Vincenti, C. H. Kruger, Introduction to physical gas dynamics,
 John Wlley & Sons, 1965.
- [24] W. Pollard, R. D. Present, On gaseous self-diffusion in long capillary
 tubes, Physical Review 73 (7) (1948) 762.
- [25] T. Hutzenlaub, J. Becker, R. Zengerle, S. Thiele, How coarsening the
 3D reconstruction of a porous material influences diffusivity and conductivity values, ECS Electrochemistry Letters 2 (2) (2013) F14–F17.
- [26] J. Lachaud, J. Scoggins, T. Magin, M. Meyer, N. Mansour, A generic local thermal equilibrium model for porous reactive materials submitted to high temperatures, International Journal of Heat and Mass Transfer 108 (2017) 1406–1417.
- ⁸¹⁸ [27] J. C. Ferguson, F. Panerai, A. Borner, N. N. Mansour, PuMA: the Porous Microstructure Analysis software, SoftwareX 7 (2018) 81–87.

- [28] W. E. Lorensen, H. E. Cline, Marching cubes: A high resolution 3D surface construction algorithm, SIGGRAPH Comput. Graph. 21 (4) (1987) 163–169.
- [29] E. V. Chernyaev, Marching cubes 33: Construction of topologically
 correct isosurfaces, Institute for High Energy Physics, Moscow, Russia,
 Report CN/95-17 42 (1995).
- [30] G. L. Vignoles, M. Donias, C. Mulat, C. Germain, J.-F. Delesse, Simplified marching cubes: An efficient discretization scheme for simulations of deposition/ablation in complex media, Computational Materials Science 50 (3) (2011) 893–902.
- [31] J. Ahrens, B. Geveci, C. Law, C. Hansen, C. Johnson, Paraview: An
 end-user tool for large-data visualization, The visualization handbook
 717 (2005).
- [32] P. Cignoni, F. Ganovelli, C. Montani, R. Scopigno, Reconstruction of
 topologically correct and adaptive trilinear isosurfaces, Computers &
 Graphics 24 (3) (2000) 399–418.
- [33] T. Lewiner, H. Lopes, A. W. Vieira, G. Tavares, Efficient implementation of marching cubes' cases with topological guarantees, Journal of graphics tools 8 (2) (2003) 1–15.
- [34] S. Van der Walt, J. L. Schönberger, J. Nunez-Iglesias, F. Boulogne, J. D.
 Warner, N. Yager, E. Gouillart, T. Yu, scikit-image: image processing
 in python, PeerJ 2 (2014) e453.
- E. Ferrié, J.-Y. Buffiere, W. Ludwig, A. Gravouil, L. Edwards, Fatigue crack propagation: In situ visualization using x-ray microtomography and 3d simulation using the extended finite element method, Acta Materialia 54 (4) (2006) 1111–1122.
- [36] I. Watson, P. Lee, R. Dashwood, P. Young, Simulation of the mechanical properties of an aluminum matrix composite using x-ray microtomography, Metallurgical and Materials Transactions A 37 (3) (2006)
 551–558.
- [37] K. Madi, S. Forest, M. Boussuge, S. Gailliègue, E. Lataste, J.-Y.
 Buffiere, D. Bernard, D. Jeulin, Finite element simulations of the deformation of fused-cast refractories based on x-ray computed tomography,
 Computational Materials Science 39 (1) (2007) 224–229.
- [38] S. Haussener, P. Coray, W. Lipiński, P. Wyss, A. Steinfeld,
 Tomography-based heat and mass transfer characterization of reticulate porous ceramics for high-temperature processing, Journal of Heat
 Transfer 132 (2) (2010).

- [39] F. Panerai, J. Ferguson, J. Lachaud, A. Martin, M. J. Gasch, N. N.
 Mansour, Analysis of fibrous felts for flexible ablators using synchrotron hard x-ray micro-tomography, in: 8th European Symposium on Aerothermodynamics for Space Vehicles, 2015.
- [40] F. Panerai, J. C. Ferguson, J. Lachaud, A. Martin, M. J. Gasch, N. N.
 Mansour, Micro-tomography based analysis of thermal conductivity,
 diffusivity and oxidation behavior of rigid and flexible fibrous insulators,
 International Journal of Heat and Mass Transfer 108 (2017) 801–811.
- [41] F. Semeraro, J. C. Ferguson, F. Panerai, R. J. King, N. N. Mansour,
 Anisotropic analysis of fibrous and woven materials part 1: Estimation of local orientation, Computational Materials Science 178 (2020)
 109631.
- [42] F. Semeraro, J. C. Ferguson, M. Acin, F. Panerai, N. N. Mansour,
 Anisotropic analysis of fibrous and woven materials part 2: Computation of effective conductivity, Computational Materials Science 186
 (2021) 109956.
- V. Koivu, M. Decain, C. Geindreau, K. Mattila, J.-F. Bloch, M. Kataja, Transport properties of heterogeneous materials. combining computerised x-ray micro-tomography and direct numerical simulations, International Journal of Computational Fluid Dynamics 23 (10) (2009) 713–721.
- [44] S. Hasanpour, M. Hoorfar, A. Phillion, Characterization of transport phenomena in porous transport layers using x-ray microtomography,
 Journal of Power Sources 353 (2017) 221–229.
- [45] A. Borner, F. Panerai, N. N. Mansour, High temperature permeability
 of fibrous materials using direct simulation Monte Carlo, International
 Journal of Heat and Mass Transfer 106 (2017) 1318–1326.
- [46] R. Jambunathan, D. A. Levin, A. Borner, J. C. Ferguson, F. Panerai,
 Prediction of gas transport properties through fibrous carbon preform
 microstructures using direct simulation monte carlo, International Journal of Heat and Mass Transfer 130 (2019) 923–937.
- 889 [47] S. Cooper, A. Bertei, P. Shearing, J. Kilner, N. Brandon, Taufactor:
 890 An open-source application for calculating tortuosity factors from to891 mographic data, SoftwareX 5 (2016) 203–210.
- [48] T. Tranter, M. Kok, M. Lam, J. Gostick, pytrax: A simple and efficient
 random walk implementation for calculating the directional tortuosity
 of images, SoftwareX 10 (2019) 100277.

- [49] G. Vignoles, Modelling binary, knudsen and transition regime diffusion
 inside complex porous media, Le Journal de Physique IV 5 (C5) (1995)
 C5-159.
- [50] T.-T. Nguyen, A. Demortière, B. Fleutot, B. Delobel, C. Delacourt, S. J. Cooper, The electrode tortuosity factor: why the conventional tortuosity factor is not well suited for quantifying transport in porous li-ion battery electrodes and what to use instead, npj Computational Materials 6 (1) (2020) 1–12.
- [51] H. Xu, J. Zhu, D. P. Finegan, H. Zhao, X. Lu, W. Li, N. Hoffman,
 A. Bertei, P. Shearing, M. Z. Bazant, Guiding the design of heterogeneous electrode microstructures for li-ion batteries: Microscopic imaging, predictive modeling, and machine learning, Advanced Energy Materials (2021) 2003908.
- S. Schmideder, L. Barthel, H. Müller, V. Meyer, H. Briesen, From three-dimensional morphology to effective diffusivity in filamentous fungal pellets, Biotechnology and bioengineering 116 (12) (2019) 3360–3371.
- 911 [53] N. N. Mansour, F. Panerai, A. Martin, D. Y. Parkinson, A. A. MacDow-912 ell, T. Fast, G. Vignoles, J. Lachaud, A new approach to light-weight 913 ablators analysis: from micro-tomography measurements to statistical 914 analysis and modeling, in: Proc. 44th AIAA Thermophysics Confer-915 ence, American Institute of Aeronautics and Astronautics, AIAA, Vol. 916 2768, 2013.
- [54] A. MacDowell, D. Parkinson, A. Haboub, E. Schaible, J. Nasiatka,
 C. Yee, J. Jameson, J. Ajo-Franklin, C. Brodersen, A. McElrone, X-ray
 micro-tomography at the Advanced Light Source, in: Developments in
 X-Ray Tomography VIII, Vol. 8506, International Society for Optics
 and Photonics, 2012, p. 850618.
- [55] F. Panerai, J. D. White, T. J. Cochell, O. M. Schroeder, N. N. Mansour,
 M. J. Wright, A. Martin, Experimental measurements of the permeability of fibrous carbon at high-temperature, International Journal of Heat
 and Mass Transfer 101 (2016) 267–273.
- [56] D. Gürsoy, F. De Carlo, X. Xiao, C. Jacobsen, Tomopy: a framework for
 the analysis of synchrotron tomographic data, Journal of synchrotron
 radiation 21 (5) (2014) 1188–1193.
- [57] D. M. Pelt, D. Gürsoy, W. J. Palenstijn, J. Sijbers, F. De Carlo, K. J.
 Batenburg, Integration of tomopy and the astra toolbox for advanced
 processing and reconstruction of tomographic synchrotron data, Journal of synchrotron radiation 23 (3) (2016) 842–849.

- J. Schindelin, I. Arganda-Carreras, E. Frise, V. Kaynig, M. Longair,
 T. Pietzsch, S. Preibisch, C. Rueden, S. Saalfeld, B. Schmid, et al., Fiji:
 an open-source platform for biological-image analysis, Nature methods
 (7) (2012) 676.
- [59] J. C. Ferguson, F. Panerai, J. Lachaud, N. N. Mansour, Theoretical
 study on the micro-scale oxidation of resin-infused carbon ablators,
 Carbon (2017).
- [60] M. R. Hestenes, E. Stiefel, Methods of conjugate gradients for solving
 linear systems, Vol. 49, NBS Washington, DC, 1952.
- [61] J. C. Ferguson, F. Panerai, J. Lachaud, A. Martin, S. C. Bailey, N. N.
 Mansour, Modeling the oxidation of low-density carbon fiber material
 based on micro-tomography, Carbon 96 (2016) 57–65.
- [62] L. Dagum, R. Menon, OpenMP: an industry standard API for shared memory programming, Computational Science & Engineering, IEEE
 5 (1) (1998) 46–55.
- J. Becker, C. Wieser, S. Fell, K. Steiner, A multi-scale approach to
 material modeling of fuel cell diffusion media, International Journal of
 Heat and Mass Transfer 54 (7) (2011) 1360–1368.
- 951 [64] A. Einstein, Investigations on the theory of the Brownian movement, 952 Courier Corporation, 1956.
- 953 [65] Z.-X. Sun, Z. Tang, Y.-L. He, W.-Q. Tao, Proper cell dimension and 954 number of particles per cell for DSMC, Computers & Fluids 50 (1) 955 (2011) 1–9.
- [66] M. A. Gallis, J. R. Torczynski, S. J. Plimpton, D. J. Rader, T. Koehler,
 Direct simulation monte carlo: The quest for speed, Proceedings of the
 29th Rarefied Gas Dynamics (RGD) Symposium 1628 (1) (2014) 27–36.
- [67] S. Plimpton, S. Moore, A. Borner, A. Stagg, T. Koehler, J. Torczynski,
 M. Gallis, Direct simulation monte carlo on petaflop supercomputers
 and beyond, Physics of Fluids 31 (8) (2019) 086101.
- [68] S. Chapman, T. G. Cowling, The mathematical theory of non-uniform
 gases: an account of the kinetic theory of viscosity, thermal conduction
 and diffusion in gases, Cambridge university press, 1970.
- [69] J. Schindelin, I. Arganda-Carreras, E. Frise, V. Kaynig, M. Longair,
 T. Pietzsch, S. Preibisch, C. Rueden, S. Saalfeld, B. Schmid, J.-Y. Tinevez, D. J. White, V. Hartenstein, K. Eliceiri, P. Tomancak, A. Cardona, Fiji: an open-source platform for biological-image analysis, Nature Methods 9 (7) (2012) 676–682. doi:10.1038/nmeth.2019.

- 970 [70] J. B. Scoggins, T. E. Magin, Development of mutation++: Multicom-971 ponent thermodynamic and transport properties for ionized plasmas 972 written in c++, in: 11th AIAA/ASME joint thermophysics and heat 973 transfer conference, 2014, p. 2966.
- 974 [71] J. B. Scoggins, V. Leroy, G. Bellas-Chatzigeorgis, B. Dias, T. E. Magin,
 975 Mutation++: Multicomponent thermodynamic and transport proper976 ties for ionized gases in c++, SoftwareX 12 (2020) 100575.
- [72] I. Wald, S. Woop, C. Benthin, G. S. Johnson, M. Ernst, Embree: a
 kernel framework for efficient CPU ray tracing, ACM Transactions on
 Graphics (TOG) 33 (4) (2014) 143.
- [73] I. Wald, G. P. Johnson, J. Amstutz, C. Brownlee, A. Knoll, J. Jeffers,
 J. Gunther, P. Navratil, OSPRay-A CPU Ray Tracing Framework for
 Scientific Visualization, IEEE transactions on visualization and computer graphics 23 (1) (2017) 931–940.

Appendix A1: Calculation of effective diffusion coefficients

In this example, we calculate the effective diffusion coefficient inside of a porous material based on the materials tortuosity, length scale, and bulk transport properties of the gas. This example is relevant to a volume-averaged simulation of mass transfer in porous media, where the user knows the tortuosity and length scale of the porous material from micro-scale simulations, but needs to compute the effective diffusion coefficient of each species in the mixture for a given set of conditions (temperature, pressure, composition).

The first step, which need only be performed once for each material, is to compute the diffusive tortuosity factor and length scale of the porous material from direct simulation on the materials micro-structure (see Sec. 4). These simulations can be performed in the PuMA software [27]. For this example, we will use a material microstructure generated from PuMA: randomly oriented intersecting cylinders. The material, shown in Fig. 14, is transverse isotropic, meaning that the material properties are isotropic in the XY plane, but variable between the XY and Z directions. A 3D tiff of the microstructure is included in the supplemental materials. The void phase is contained in the grayscale values of 0 to 127, and the solid phase is contained within values 128 to 255. The material porosity is 0.875.

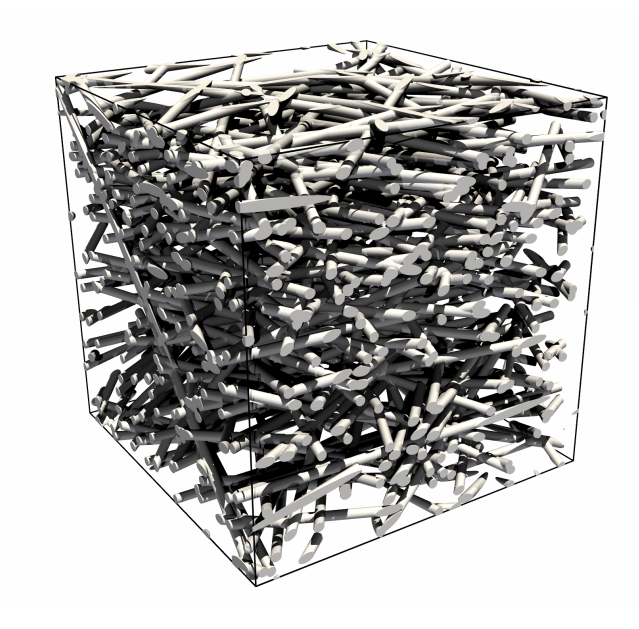


Figure 14: Computationally generated transverse isotropic microstructure of intersecting cylinders

The tortuosity factors were calculated in PuMA using the random walk method for both the continuum and rarefied simulations. For both sim-

ulations, 100,000 particles were used for a total walk distance of 100,000 voxels per particle. The tortuosity and length scales were calculated following the procedure at the end of Sec. 4.2. The X and Y values were averaged, resulting in the following values for the tortuosity and the length scale:

Direction
$$\eta$$
 $l_D(m)$
XY 1.0727 6.292 · 10⁻⁵
Z 1.1319 4.678 · 10⁻⁵

Now that the material tortuosity and length scale has been determined, we will pick an example set of conditions to calculate the effective diffusion coefficient within the porous material. For this example, we will use an equimolar Argon-Xenon mixture at 0.001 atm and 273.15K. Within your volume averaged simulation tool, the bulk properties (independent of the porous media) for the mixture need to be computed. These properties should require little computational time to determine, and can be computed using a number of tools, such as mutation++ [70, 71]. In this example, we calculate the bulk properties using the DSMC tool SPARTA [67]. The properties of interest are the mean thermal velocity, and the bulk diffusion coefficient of the species into the mixture:

Species
$$\bar{v}$$
 (m/s) $D_{\text{bulk}}^{\text{j} \to \text{mix}}$ (m²/s)
Ar 380.241 $1.174 \cdot 10^{-2}$
Xe 209.315 $6.334 \cdot 10^{-3}$

Now, we use Eq. 10 and 11 to determine the reference and effective diffusion coefficients in the material, in m^2/s :

Species
$$D_{\text{ref}}^{\text{XY}}$$
 $D_{\text{eff}}^{\text{XY}}$ $D_{\text{ref}}^{\text{Z}}$ $D_{\text{ref}}^{\text{Z}}$ $D_{\text{eff}}^{\text{Z}}$

Ar \rightarrow mix $4.749 \cdot 10^{-3}$ $3.873 \cdot 10^{-3}$ $3.939 \cdot 10^{-3}$ $3.045 \cdot 10^{-3}$

Xe \rightarrow mix $2.593 \cdot 10^{-3}$ $2.115 \cdot 10^{-3}$ $2.154 \cdot 10^{-3}$ $1.665 \cdot 10^{-3}$

Finally, we compare the above results to direct numerical simulation of an Argon-Xenon mixture in the porous media, simulated using the SPARTA DSMC solver, in m²/s:

Comparing our model results to the direct numerical simulation, we have excellent agreement with an average percent difference of 1.14%.

Appendix A2: Computationally generated microstructures

We used four types of artificially generated geometries: a capillary tube, 1D cylinders, 3D cylinders, and 3D packed sphere beds. These geometries are used in classical studies of tortuosity in porous media [16, 17, 22] and allow us to compare with the literature. The same geometry storage method is used for the computationally generated materials as was used for the X-ray microtomography datasets: a 3D matrix of grayscale values at each voxel, with a threshold value used to segment void from material. These four geometries consist of two primitive shapes - cylinders and spheres.

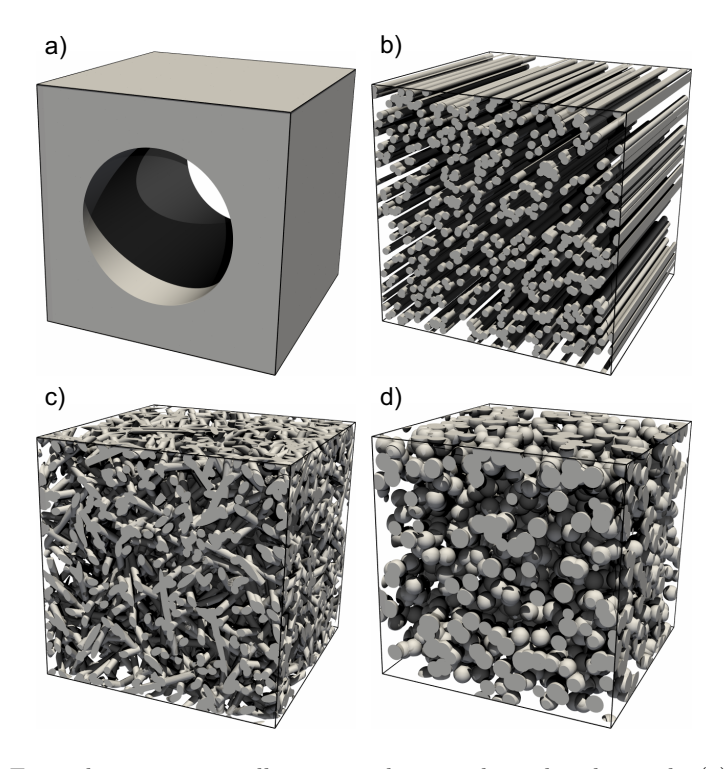


Figure 15: Example computationally generated materials used in this work: (a) a capillary, (b) 1D cylinders, (c) 3D cylinders, and (d) a packed sphere bed. Visualizations performed in ParaView [31] with the OSPRay ray-tracer [72, 73].

To generate a sphere on a continuous Cartesian grid, a centerpoint and radius is chosen, and each voxel in the vicinity is assigned a grayscale value between 0 and 255 based on its distance to the centerpoint. To generate a random sphere bed, spheres are generated at random centerpoints until the desired porosity is met.

To generate a cylinder on a continuous Cartesian grid, a center line segment and radius is chosen, and each voxel in the vicinity is assigned a value based on its distance to the line segment. Random 1D structures are generated by creating parallel cylinders until the desired porosity is reached.

For a random 3D structure, random positions and angles are assigned to each generated cylinder, until the desired porosity is reached. Periodic boundary conditions are used for all random generated structures in the event that a primitive shape extends past the domain.

An example of each computationally generated structure is shown in Fig. 15, with each of the random structures having a porosity of 0.7. For fiber and sphere geometries (Fig. 15(b), (c), and (d)) overlap and intersections are allowed between the elements, though PuMA allows for the generation of microstructures with non overlapping elements as well.

